FISEVIER

Contents lists available at ScienceDirect

Earth and Planetary Science Letters

www.elsevier.com/locate/epsl



Systematic heat flow measurements across the Wagner Basin, northern Gulf of California



Florian Neumann ^a, Raquel Negrete-Aranda ^{b,*}, Robert N. Harris ^c, Juan Contreras ^b, John G. Sclater ^d, Antonio González-Fernández ^b

- a Posgrado en Ciencias de la Tierra, Centro de Investigación Científica y de Educación Superior de Ensenada, Ensenada, BC, 22864, Mexico
- ^b Departamento de Geología, Centro de Investigación Científica y de Educación Superior de Ensenada, Ensenada, BC, 22864, Mexico
- ^c College of Earth, Ocean, and Atmospheric Sciences, Oregon State University, Corvallis, OR 97331, USA
- d Geosciences Research Division, Scripps Institution of Oceanography, UC San Diego, La Jolla, CA, 92093-0220, USA

ARTICLE INFO

Article history: Received 1 March 2017 Received in revised form 13 September

Accepted 14 September 2017 Available online 6 October 2017 Editor: R. Bendick

Keywords: Gulf of California extensional province narrow rift continental rupture distributed deformation advective heat transport

ABSTRACT

A primary control on the geodynamics of rifting is the thermal regime. To better understand the geodynamics of rifting in the northern Gulf of California we systematically measured heat-flow across the Wagner Basin, a tectonically active basin that lies near the southern terminus of the Cerro Prieto fault. The heat flow profile is 40 km long, has a nominal measurement spacing of \sim 1 km, and is collocated with a seismic reflection profile. Heat flow measurements were made with a 6.5-m violin-bow probe. Although heat flow data were collected in shallow water, where there are significant temporal variations in bottom water temperature, we use CTD data collected over many years to correct our measurements to yield accurate values of heat flow. After correction for bottom water temperature, the mean and standard deviation of heat flow across the western, central, and eastern parts of the basin are 220 \pm $60,\,99\pm14,\,889\pm419~\text{mW}\,\text{m}^{-2}$, respectively. Corrections for sedimentation would increase measured heat flow across the central part of basin by 40 to 60%. We interpret the relatively high heat flow and large variability on the western and eastern flanks in terms of upward fluid flow at depth below the seafloor, whereas the lower and more consistent values across the central part of the basin are suggestive of conductive heat transfer. Moreover, heat flow across the central basin is consistent with gabbroic underplating at a depth of 15 km and suggests that continental rupture here has not gone to completion.

© 2017 Elsevier B.V. All rights reserved.

1. Introduction

The Gulf of California (GC) is a natural laboratory to study the transition from continental rifting to rupture and seafloor spreading (Fig. 1). The GC is a 1200 km long transtensional rift system between Baja California, a sliver of continental lithosphere on the Pacific plate, and the western margin of the North-American plate. The GC bridges the right lateral continental San Andreas Fault system in the north with the oceanic East Pacific Rise in the south through a series of long transforms linking short rift basins (Lonsdale, 1989). Although the GC transitions from well-developed oceanic spreading in the Salton Trough, this transition does not appear to vary systematically along strike.

Extension in the Gulf began 12–12.5 Myr ago when subduction of the Farallon plate ended west of Baja California (Lonsdale, 1989, 1991; Stock and Lee, 1994a 1994b; Umhoefer, 2011). Oblique rifting of the GC began synchronously at \sim 6 Ma, resulting in at least 255 \pm 10 km of transform displacement along the northern Gulf of California (Oskin et al., 2001; Oskin and Stock, 2003; Dorsey et al., 2007). Despite synchronous opening and similar magnitudes of extension, rifting vary from south to north including mode of deformation, oceanic crustal thickness and width, and magmatism volume (Lizarralde et al., 2007).

In the southern and central GC continental rupturing is complete. The southern GC consists of the Alarcon Farallon, and Pescadero Basins. The Alarcon Basin in the southern Gulf is the only basin to exhibit magnetic lineations characteristic of normal oceanic crust (Larson et al., 1972; Klitgord et al., 1974; DeMets, 1995). Here, the onset of seafloor spreading is estimated to have occurred 2–3 Myr ago and has accommodated approximately 135 km of new oceanic crust with a thickness of 6 km (Lizarralde et al., 2007). North of the Alarcon Basin, the Farallon

^{*} Corresponding author.

E-mail address: rnegrete@cicese.mx (R. Negrete-Aranda).

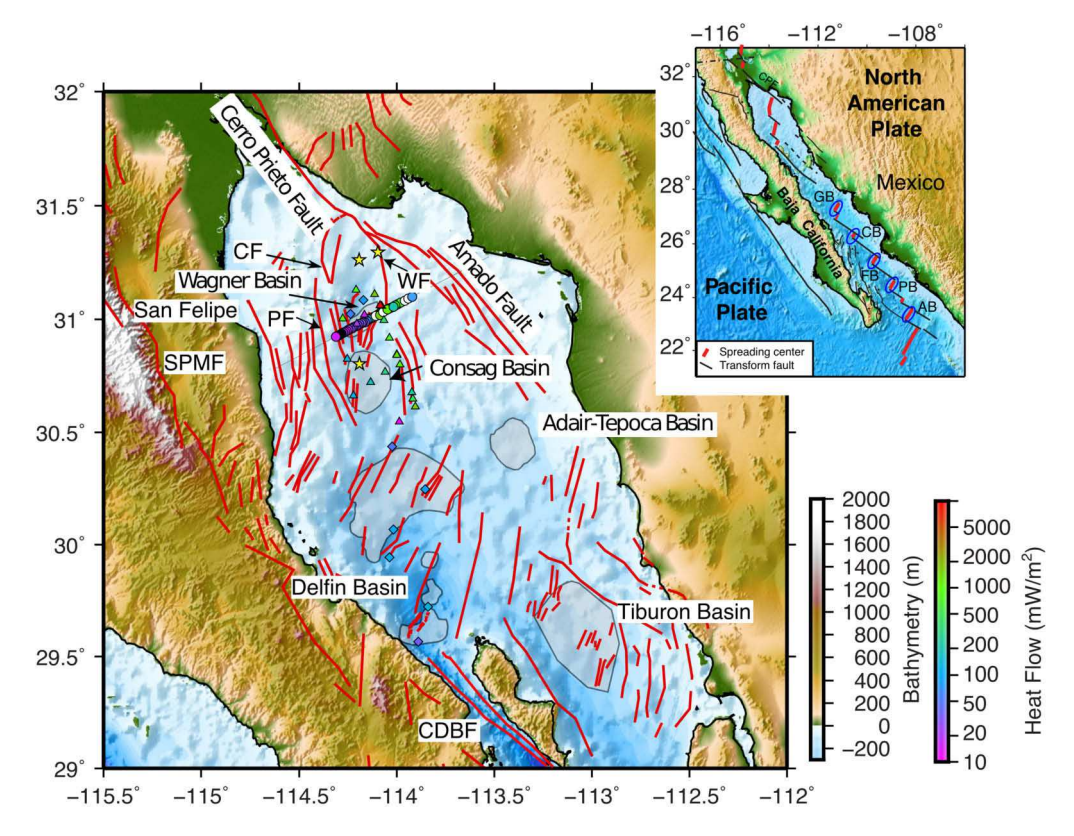


Fig. 1. Elevation and bathymetry map of the northern Gulf of California showing the distribution of rift basins and faults in the region (red lines). Fault traces are from Persaud et al. (2003), Aragón-Arreola and Martín-Barajas (2007), Plattner et al. (2007), González-Escobar et al. (2009), Martín-Barajas et al. (2013). Circles are new heat flow measurements collected for this study; Triangles and squares represent heat flow data from Prol-Ledesma et al. (2013) and Henyey and Bischoff (1973) respectively; circle color is proportional to heat flow magnitude, white circles show the partial penetrations. Black line across the Gulf of California is the location of a regional seismic reflection line collected by PEMEX and processed by Aragón-Arreola and Martín-Barajas (2007). Stars represent boreholes drilled by PEMEX. Abbreviations: WF = Wagner Fault; PF = Percebo Fault; CF = Consag Fault; SPMF = San Pedro Mártir Fault; CDBF = Canal de Ballenas Fault; Southern basins on inset map: AB = Alarcón Basin; PB = Pescadero Basin; FB = Farallon Basin; CB = Guaymas Basin. (For interpretation of the references to color in this figure, the reader is referred to the web version of this article.)

and Pescadero Basins show incipient spreading centers. In the central Gulf, at the Guaymas Basin continental rupture is estimated to have occurred 6 My ago and \sim 280 km of new oceanic crust has accommodated the extension; seismic reflection data show that the oceanic crust is 6–9 km thick and rapid shallowing of the Moho across the continental oceanic transition characteristic of narrow rifts (Lizarralde et al., 2007).

North of the Guaymas Basin, the upper Delfin and Tiburon basin show crustal thicknesses of 14 and 17 km respectively (González-Fernández et al., 2005). On the basis of extension estimates and an analysis of synrift sedimentation and magmatism, Martín-Barajas et al. (2013) inferred that lithospheric rupture across the Tiburon is not complete. Just to the north, the Upper and Lower Delfin basins have ruptured and 40–70 km wide new hybrid oceanic crust, consisting of gabbro and differentiated igneous rocks intruding the sedimentary cover, has been emplaced (Persaud et al., 2003; González-Fernández et al., 2005). The situation in the Wagner basin is less clear because of thick sediment accumulation (>7 km) and the lack of deep crustal imaging.

Between the Salton Trough to the north and the Delfin Basins to the south, the northern GC is currently hosting the transition from continental rifting to rupture (Fig. 1). In the Wagner Basin it is unclear whether the lithosphere has ruptured or not. Prol-Ledesma et al. (2013) report widely spaced heat flow values that range between 16 and >15,000 mW m $^{-2}$. Most of the very high values of heat flow are along the Wagner Fault system that cuts the eastern margin of the basin. Prol-Ledesma et al. (2013) interpret the high mean heat flow of 1875 mW m $^{-2}$ as evidence of continental rupture and active seafloor spreading. However, this interpretation is at odds with observations and models of distributed deformation between the Cerro Prieto and Canal de Ballenas transform faults (Persaud et al., 2003, 2016).

To better understand the thermal regime of the Wagner basin and processes associated with continent rupture, we undertook a program of systematic heat flow measurements. Here we focus on a single heat flow profile (Fig. 1) acquired on board the R/V Alpha Helix in 2015. We use these values coupled with isostatic considerations to argue that continental rupture within the Wagner Basin is not yet complete.

2. Northern Gulf of California and the Wagner basin

In the northern Gulf, there are several tectonically active and inactive rift basins (Aragón-Arreola and Martín-Barajas, 2007; González-Escobar et al., 2009; Martín-Barajas et al., 2013). The group of inactive rifts is located along the eastern part of the Gulf and comprises Adair, Tepoca and Tiburón basins (Fig. 1). At \sim 6 Ma, active rifting jumped westward from the now inactive rift basins to form the currently active rift basins that include the Wagner, Con-

sag, Upper Delfin, and Lower Delfin basins. This region is bounded by two major regional right-lateral transform faults. To the northeast, the Cerro Prieto fault with down throw to the west marks the western limit of the Altar Basin (Aragón-Arreola and Martín-Barajas, 2007). To the southwest, the Canal de Ballenas Transform fault can be traced north to the Lower Delfin Basin. In this area, the Canal de Ballenas Fault splits into several segments forming horsetails structures (Persaud et al., 2003).

The Wagner and Consag basins are the northernmost and shallowest of the active basins in the GC, with maximum depths of \sim 225 m. These basins are connected and controlled by the NNW Wagner Fault, which branch out from the Cerro Prieto transform fault. Subsidence is controlled by shallow fault arrays rooted in the Wagner Fault, and sediments on it show fault propagation folds (Aragón-Arreola and Martín-Barajas, 2007).

In this region, fault scarps are smaller and less common than in other major basins, but the density of faults is higher in the Wagner Basin than in the Upper Delfin Basin (Persaud et al., 2003). The structural pattern is asymmetric, with more active faults over a broader region in the SE flank of the basin and a narrower, less active fault zone in the NW side of the basin (Persaud et al., 2003).

These basins contain a syntectonically deposited sequence of sediments that is at least 7 km thick (Pérez, 1980; Persaud et al., 2003; Aragón-Arreola and Martín-Barajas, 2007; González-Fernández et al., 2005, 2009). Wells drilled by the Mexican Oil Company (PEMEX) penetrated ~5 km of Pleistocene sediments, below which the ages were either undetermined or Pleistocene (Helenes et al., 2009). In general, the sediment mainly consists of a mixture of fine sand and silt. The sand at times is very clean and is arranged in massive strata up to 2 m thick. The silt occurs in bundles of laminae, several meters thick.

3. Heat flow across the Wagner basin

We present 33 temperature-depth profiles (Fig. 3 and Table 1) from the Wagner Basin collected on the R/V Alpha Helix in 2015. Of the 33 measurements, 5 are partial penetrations that do not yield reliable values of heat flow. Heat flow measurements were made with a FIELAX multi-penetration heat flow probe based on the violin bow design that provides both the mechanical robustness to withstand repeated insertions and withdrawals from the sediment, and sensitivity needed to make highly accurate measurements. The thermistor string is 6-m long and houses 22 thermistors of 1 mK precision. Other parameters measured by the system include time, pressure (depth), water temperature, tilt, and a stable reference resistance.

Heat flow measurements were collocated with seismic reflection profile 5037 (Fig. 1), acquired by PEMEX and processed by Aragón-Arreola and Martín-Barajas (2007). Echo sounder profiles were also collected during the cruise. Spacing between each measurement is nominally 1 km but decreases to approximately 500 m around targets of interest (Fig. 1).

All heat flow determinations are processed based on the formulation described by Hartmann and Villinger (2002). Probe insertion into the sediment generates a frictional heat pulse whose decay is described by a cylindrical source. We compute equilibrium temperatures by fitting the time series to a cylindrical decay curve over a 10-min time period and extrapolating to infinite time. After the initial 10 min time period a 20 s calibrated heat pulse of 1 kJ m⁻¹ (Lister, 1979) is generated and the temperature decay is used to estimate the in situ thermal conductivity. The mean thermal conductivity over the transect is 1.16 W m⁻¹ K⁻¹ and the standard deviation of the measurements is 0.28 W m⁻¹ K⁻¹. Moreover, thermal conductivity-depth profiles generally show a slight increase of this material parameter with depth (Fig. 2).

The temperature-depth profiles (Fig. 3) show two conspicuous features. The first feature is the large thermal gradients and the second is curvature in the shallow sub-bottom profiles. Also note the short wavelength variability in the gradients associated with the eastern Wagner Basin. Possible sources of curvature include the effects of bottom water temperature variation (BWT), bathymetry and the advective transport of heat caused by sedimentation and fluid flow. These issues are discussed in the following sections.

3.1. Bottom water temperature variations

A challenge in interpreting heat flow data in shallow water is removing the influence of temporal variations in BWT. The shallow water depths (<250 m) of the Wagner Basin are susceptible to large temporal variations in BWT that can produce significant curvature. Unfortunately, time-series of BWT prior to and during the period of the experiment are not available for the northern GC. We explore the nature of BWT variations using studies of sea surface temperature (SST) and CTD casts available from the NOAA database (Levitus et al., 2013) and CICESE (Godínez et al., 2013).

Lavín and Marinone (2003) used satellite infrared images collected between January 1984 and December 2000 to analyze SST anomalies. Their analysis indicates maximum SST between July and August and minimum SST between January and March. An empirical orthogonal function analysis shows that the first mode explains 97% of the variability. The time evolution of this mode is strongly sinusoidal with an annual period due to seasonal heating and cooling combined with tidal mixing (Lavín and Marinone, 2003). The annual harmonic accounts for 95% of the SST variability in the northern GC. Thermodynamic studies of the northern GC indicate the water around the Wagner Basin is only weakly stratified (e.g., Montes et al., 2015). Mixing occurs through the combined effects of thermohaline circulation, tidal mixing and coastal upwelling (Alvarez-Borrego and Lara-Lara, 1991). Vertical mixing induced by tidal currents in the northern Gulf is strong because the length of the gulf is shorter than a half wavelength of the semidiurnal tidal harmonics so that the gulf are almost resonant at the frequency (Argote et al., 1995). These results suggest the dominant variability in BWT is at the annual time scale.

To check this result, we compiled CTD casts available from the NOAA database (Levitus et al., 2013) and CICESE (Godínez et al., 2013). Over 1163 CTD casts exist between 1980 and 2015, though most of the casts were recorded between 1984 and 2004 (Fig. 4a). We averaged temperatures at 50, 100, 150, and 200 m depth and plotted them as a function of month for all available years (Fig. 4d). A sinusoid with an annual period fits the data well for all depths but amplitude and phase must decay with depth to explain the data properly, consistent with the physical oceanography studies discussed previously. At 200 m depth, the amplitude of the variation is small at 0.24°C, and the root-mean-square (RMS) misfit shows little sensitivity to the phase. Variations in BWT shorter than one month produce perturbations in the sub-bottom that diffuse away at shallow depths. For a monthly variation the fluctuation decreases to 1/e of the BWT at a depth of approximately 0.6 m. We checked for long-wavelength variations by plotting the CTD temperatures as a function of time for depths of 150 m and 200 m. Linear trends to this data are not statistically significant. These analyses suggest that the dominant period of BWT variation is at the annual time scale and that extreme BWT temperatures are in winter and summer months, respectively.

We show the vertical temperature structure of the water column using a subset of CTDs in the immediate vicinity of Wagner Basin (Fig. 4a). Water column temperature profiles based on these casts vary from about 16.4° to 31° C at the surface and diminish to 13.4° to 16.4° C at a depth of 200 m (Fig. 5a). Fig. 5a also shows the mean BWT measured at the top of the probe during each pen-

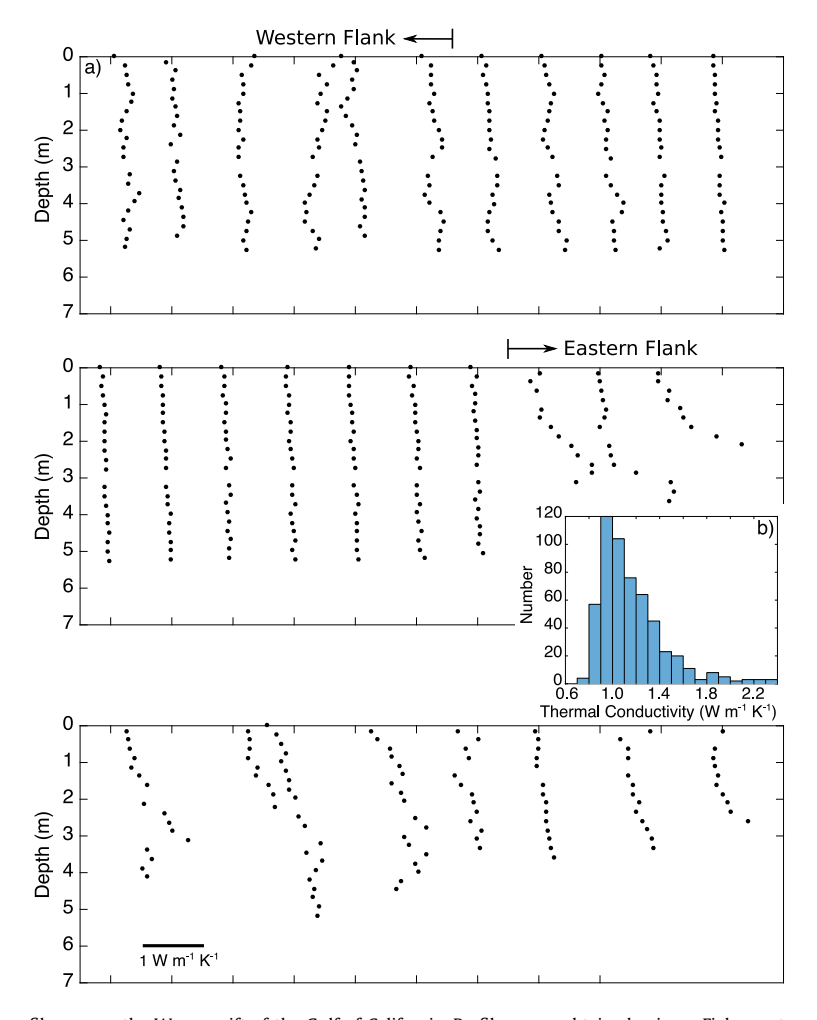


Fig. 2. Thermal conductivity-depth profiles across the Wagner rift of the Gulf of California. Profiles were obtained using a Fielax system of 22 thermistors along a thermistor string 6 m long. Thermistor 10 was removed from the profiles because of thermal perturbations caused by a mount point of the probe. We assumed conductivities for penetrations 25 and 29 based on neighboring profiles and are not shown.

etration plotted as a function of water depth. These values follow a depth trend similar to that observed in the CTD casts. The standard deviation of these temperatures is plotted as a function of depth (Fig. 5b) and gives a rough sense of what BWT variation might be.

Consistent with the above analysis we assume that BWT variations are dominantly sinusoidal at the annual time scale and that the temperature profile can be described by,

$$T_{pred}(z,t) = T_0 + q_0 \sum_{i=1}^{N} \frac{\Delta z_i}{k(z)_i} + \Delta T \exp(-\xi) \cos\left(\frac{2\pi}{\tau}t - \xi\right)$$
 (1)

where T is temperature, z is depth, t is time, T_0 is surface temperature intercept, q_0 is the surface heat flow, k is the thermal conductivity, ΔT is the amplitude of the BWT variation, and

$$\xi = \sqrt{\frac{\pi}{\tau}} \sum_{i=1}^{N} \frac{z_i}{\sqrt{k_i/\rho c}},\tag{2}$$

where τ is the period of the BWT variation, and ρc is heat capacity. Here we use a constant heat capacity of 2.36 MJ m⁻³ K⁻¹. The first two terms on the right-hand side of equation (1) describe the background, lineal thermal regime. The ratio of the depth interval to the thermal conductivity over that interval is the thermal resistance and is summed over N intervals defined by the measured data points. The third term describes the perturbations due to the BWT variation and the summation accounts for variations in thermal conductivity with subsurface depth. The exponential

term describes the attenuation of the thermal wave, which scale as the square root of the period π/τ . Short period variations attenuate away at relatively shallow depths while long period variations penetrates to greater depth. In the supplementary information we show that we can recover these parameters to a few percent.

We invert our dataset and assess the results with a number of expectations: 1) parameters should vary in a relatively smooth way across the Wagner basin; 2) the long-term bottom water temperature, T_0 should vary as a function of depth and be in accord with the CTD data; and 3) the difference between T_0 and the measured BWT from the probe should be consistent with estimates of ΔT . The goal is to produce the most reliable (unbiased) model, in which the variance of the final heat flow estimate is reduced as much as possible. Fig. 6 shows the RMS misfits between the data and model fit as well as the inverted parameters as a function of distance along the heat flow transect. RMS misfits vary between 90 and 25 mK. Inverted parameters generally vary smoothly across the western edge of the Wagner Basin and through the central portion of the basin. In contrast, on the eastern side of the basin, parameters vary in a non-systematic way and may be sensitive to a process not accounted for in our inversion. In section 3.3 we show that these data are consistent with fluid flow. Note that five penetrations in the eastern basin are incomplete with less than 11 of the 22 thermistors entering the sediment (Fig. 3). Our analysis shows that our inversion scheme does not yield reliable results for these data and these measurements are not discussed further.

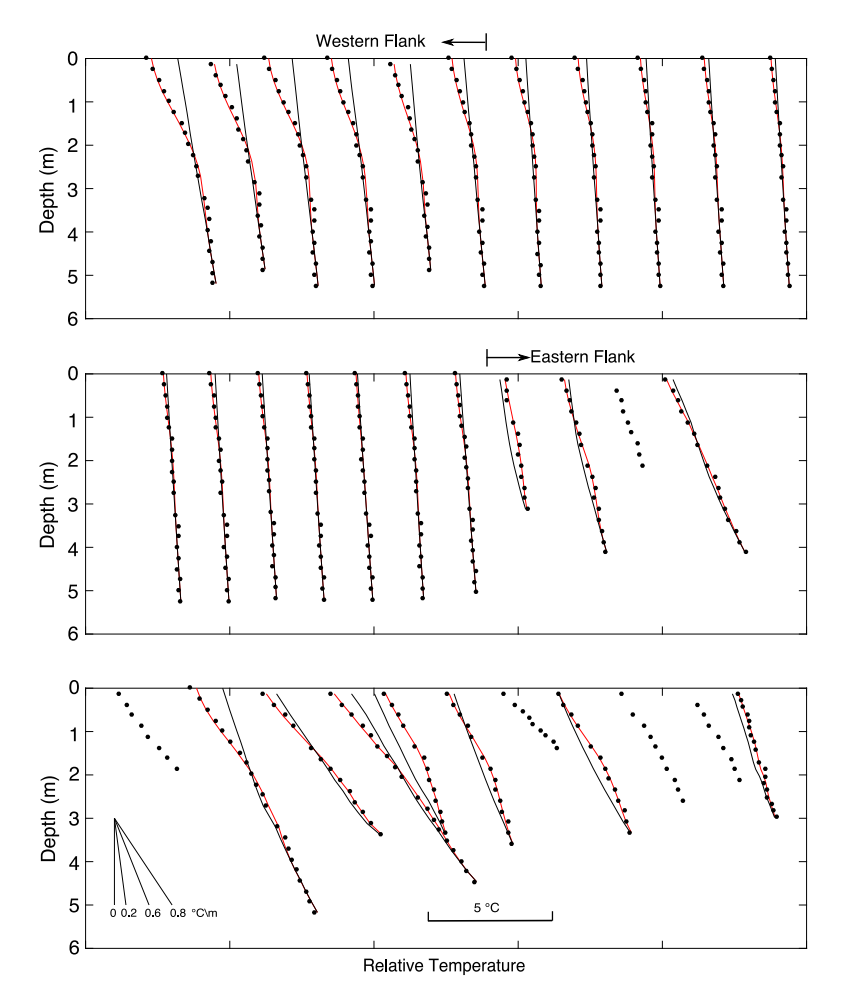


Fig. 3. Temperature-depth profiles across the Wagner rift of the Gulf of California. Profiles were obtained using a Fielax system of 22 thermistors along a thermistor string 6 m long. Thermistor 10 was removed from the profiles because of thermal perturbations caused by a mount point of the probe. Best fitting curve from the inversion model is shown in red. Black curve represents background thermal regime For the partial penetrations the poor model fit precludes the interpretation of these measurements. (For interpretation of the references to color in this figure, the reader is referred to the web version of this article.)

Fig. 6 shows that with the exception of the eastern side of the Wagner Basin our first expectation is met. We check the second two expectations by comparing our results with the CTD casts. Fig. 5a shows that the extrapolated bottom water temperature, T_0 , is in accord with the CTD casts but is offset from the instantaneous BWT measured at the top of the probe. This difference provides an estimate of the BWT amplitude, ΔT . We show these differences at an expanded scale in Fig. 5b. ΔT derived from the inversion of the temperature-depth profiles is within the standard deviation of the CTD casts and generally diminishes with water depth in accord with the CTD analysis (Fig. 5b). For depths of 50 and 200 m, characteristic of the Central Wagner Basin and its flanks, our estimated ΔT varies between 1.75 $^{\circ}$ and 0.2 $^{\circ}$ C, respectively. The central basin where the seafloor depth is the greatest shows the best agreement between ΔT and the difference between the BWT and T_0 . These differences vary between 0.6 and 0.2 °C and diminish with water depth.

Optimum heat flow values are shown in Fig. 7 and in Table 1. Uncertainties represent the 95% confidence interval. Based on the inverted parameters (Fig. 6) and the heat flow we divided our transect into three regimes, the central basin where heat flow is relatively consistent, the western portion with slightly higher heat flow, and the eastern portion where heat flow is significantly higher and more variable than the central basin. Water depths associated with the western portion range between 66 and 113 m, those in the central portion are between 127 and 202 m and those on the eastern side range between 200 and 57 m. The relatively

small uncertainties associated with measurements in the central Wagner Basin reflect the goodness of fit, whereas the large uncertainties associated with measurements on the western and eastern portions of the transect basin indicate generally poorer fits. The mean heat flow across the central basin is 99 \pm 14 mW m $^{-2}$. The estimated magnitude of bottom water variation across the basin floor is 0.5 °C, leading to an approximately 10% change in the gradient, well within the standard deviation of the data.

3.2. Sedimentation

Heat flow values are likely depressed because of the time required to warm cold sediments to the background thermal conditions. Sedimentation rates in the northern GC are not precisely known. Chronostratigraphic studies in deep (~4 km) boreholes drilled by PEMEX in the northwestern part of the Wagner basin suggest sediment accumulation rate of ~1 mm yr⁻¹ (Aragón-Arreola and Martín-Barajas, 2007; Helenes et al., 2009). Dorsey (2010) estimates an average sediment accumulation rate in the Salton Trough and NGOC of 1.9–2.3 mm yr⁻¹ based on eroded volume of rock transported by the Colorado River over the past 5–6 Myr. Moreover, observations in the Laguna Salada basin, farther north, suggest the sedimentation rate is approximately 0.7 mm yr⁻¹ (Contreras et al., 2005). We estimate the potential impact of sedimentation on heat flow values using the one dimensional advective heat transport equation

Table 1Heat flow data for the Wagner Basin.

Penetration	Longitude (deg)	Latitude (deg)	Water depth (m)	Bottom water temperature (°C)	Long-term bottom water temperature $T_0 \pm 2\sigma$ (°C)	Temperature amplitud $\Delta T \pm 2\sigma$ (°C)	Phase (month of year)	Heat flow $\pm 2\sigma$ (mW/m ²)
HF007P05	-114.3112	30.9234	66	16.65	18.20 ± 0.16	-1.01 ± 0.20	12	326 ± 56
HF007P04	-114.3022	30.9277	76	16.27	17.84 ± 0.14	-0.89 ± 0.20	9	223 ± 48
HF007P03	-114.2929	30.9320	85	15.69	17.36 ± 0.13	-0.98 ± 0.19	10	201 ± 44
HF007P02	-114.2835	30.9364	92	15.45	16.91 ± 0.12	-0.70 ± 0.16	10	237 ± 45
HF007P01	-114.2747	30.9405	102	15.42	16.66 ± 0.11	-0.64 ± 0.15	9	151 ± 34
HF006P08	-114.2653	30.9448	113	15.34	16.12 ± 0.10	-0.61 ± 0.18	1	182 ± 38
HF006P07	-114.2557	30.9488	127	15.39	15.87 ± 0.08	-0.60 ± 0.16	1	123 ± 29
HF006P06	-114.2468	30.9535	138	15.29	15.57 ± 0.07	-0.50 ± 0.14	1	121 ± 25
HF006P05	-114.2373	30.9572	163	14.61	15.24 ± 0.05	-0.37 ± 0.13	12	106 ± 20
HF006P04	-114.2279	30.9617	190	14.52	15.01 ± 0.05	0.24 ± 0.11	1	97 ± 16
HF006P03	-114.2197	30.9656	197	14.46	14.92 ± 0.05	0.21 ± 0.10	1	87 ± 16
HF006P02	-114.2093	30.9700	202	14.44	14.81 ± 0.05	0.19 ± 0.11	1	86 ± 14
HF006P01	-114.2004	30.9742	206	14.45	14.79 ± 0.06	0.18 ± 0.09	1	83 ± 16
HF005P12	-114.1916	30.9784	208	14.45	14.73 ± 0.06	0.17 ± 0.10	1	86 ± 15
HF005P11	-114.1811	30.9825	208	14.43	14.65 ± 0.05	0.12 ± 0.10	1	94 ± 14
HF005P10	-114.1731	30.9862	207	14.42	14.63 ± 0.07	0.06 ± 0.09	1	99 ± 18
HF005P09	-114.163	30.9860	200	14.50	14.75 ± 0.06	0.18 ± 0.10	1	93 ± 18
HF005P08	-114.1539	30.9945	202	14.63	14.78 ± 0.06	0.18 ± 0.09	1	111 ± 19
HF005P07	-114.1442	30.9992	200	14.66	14.46 ± 0.15	-0.69 ± 0.36	8	388 ± 54
HF005P06	-114.1349	31.0034	191	14.71	15.15 ± 0.05	0.82 ± 0.22	12	440 ± 31
HF005P05a	-114.1259	31.0072	180	14.72				
HF005P04	-114.1168	31.0111	160	14.75	15.37 ± 0.07	-0.52 ± 0.17	12	1005 ± 4
HF008P02 ^a	-114.08425	31.0200	103	15.91				
HF004P04	-114.0518	31.0415	75	16.20	17.75 ± 0.12	-1.26 ± 0.21	1	774 ± 46
HF010P03	-114.048	31.0445	75	17.00	17.62 ± 0.12	0.88 ± 0.30	11	1570 ± 9
HF004P03	-114.0426	31.0459	70	16.29	18.22 ± 0.13	-0.94 ± 0.23	12	1581 ± 7
HF004P01	-114.0233	31.0533	65	16.93	17.02 ± 0.16	-1.36 ± 0.35	10	981 ± 57
HF003P01	-114.0166	31.0564	67	16.96	17.78 ± 0.05	1.09 ± 0.21	1	637 ± 30
HF008P09 ^a	-114.0065	31.0621	62	17.23	= 5,00	0.2.	-	
HF008P010	-113.9951	31.0662	62	17.40	17.41 ± 0.06	-1.27 ± 0.23	9	913 ± 31
HF008P011 ^a	-113.9776	31.0745	59	17.53			-	
HF008P012 ^a	-113.9592	31.0828	58	17.52				
HF008P013	-113.9406	31.0912	57	17.62	17.43 ± 0.27	0.40 ± 0.40	8	602 ± 95

^a Partial penetration that does not yield a reliable model.

$$\frac{\partial^2 T}{\partial z^2} = \frac{\partial T}{\partial t} + V_s \frac{\partial T}{\partial z},\tag{3}$$

where V_s is the sedimentation rate, which we assume 1–2 mm yr $^{-1}$ over the past 5–6 Myr. This results in the depression of heat flow values by approximately 40%–60% in the central Wagner Basin from a value of \sim 150 \pm 21 mW m $^{-2}$ to the currently observed value of 99 \pm 14 mW m $^{-2}$.

3.3. Advective fluid flow

Heat flow measurements on the eastern and western sides of the Wagner basin show higher and more variable heat flow than in the central basin. The very high and variable heat flow values, especially that associated with the eastern basin, are difficult to interpret with the available information. If conductive heat transfer is responsible for the high and variable heat flow, it would need an extra source of heat that is shallow and variable. This region sits on top of a regional low shear-wave velocity anomaly (Di Luccio et al., 2014; Persaud et al., 2015, 2016), which might be the product of a thermal anomaly but the source is too deep and regional to account for the horizontal gradient in heat flow between the central and eastern portions of the Wagner Basin and we see no evidence for a shallow conductive heat source in the seismic reflection profile. This rationale leads us towards an interpretation of advective heat transfer. One possibility for advective heat transfer is fluid flow focused along permeable pathways such as faults. Indeed, the seismic reflection profile shows numerous faults that can be traced much closer to the seafloor in the eastern and western portions of the Wagner Basin than in the central part of the basin and fault offsets are observed in the eastern portion of the basin (Persaud et al., 2003). With this scenario the variability may be explained with alternating regions of fluid discharge or recharge or flow in and out of the plane of the transect.

An alternative scenario is fluid seepage caused by transient flow from arrested compaction or asymmetric loading that leads to two-dimensional flow. The sediments comprising the Wagner Basin generally consist of fine sands and silt that have relatively high permeability making the development of overpressure unlikely. Moreover, asymmetric loading of the sediments is not observed. These arguments cause us to discount fluid seepage as a source of advective heat transfer. In supplementary information 2 we argue that even if seepage is caused by overpressures from arrested compaction it is unlikely to elevate the heat flow.

To explore the implications of advective fluid flow along faults we use a simple one-dimensional steady-state model of the vertical flow through a porous media,

$$\frac{\partial^2 T}{\partial z^2} - \frac{\phi \rho_W c_W}{k_e} V_z \frac{\partial T}{\partial z} = 0 \tag{4}$$

where ϕ is porosity, k_e is the effective thermal conductivity, $\rho_w c_w$ is the heat capacity of water, and V_z is the mean vertical fluid velocity. For boundary conditions we assume an isothermal seafloor $T(z=0)=T_0$, and assume a constant thermal gradient, Γ_L at depth L, the base of the system. The solution for this model is,

$$T(z) = T_0 + \frac{\Gamma_L L}{\beta} \frac{\exp(\frac{\beta}{L}z) - 1}{\exp(\beta)},$$
 (5)

where β is the Peclet number given by,

$$\beta = \frac{\phi \rho_W c_W V_z L}{k_e}.\tag{6}$$

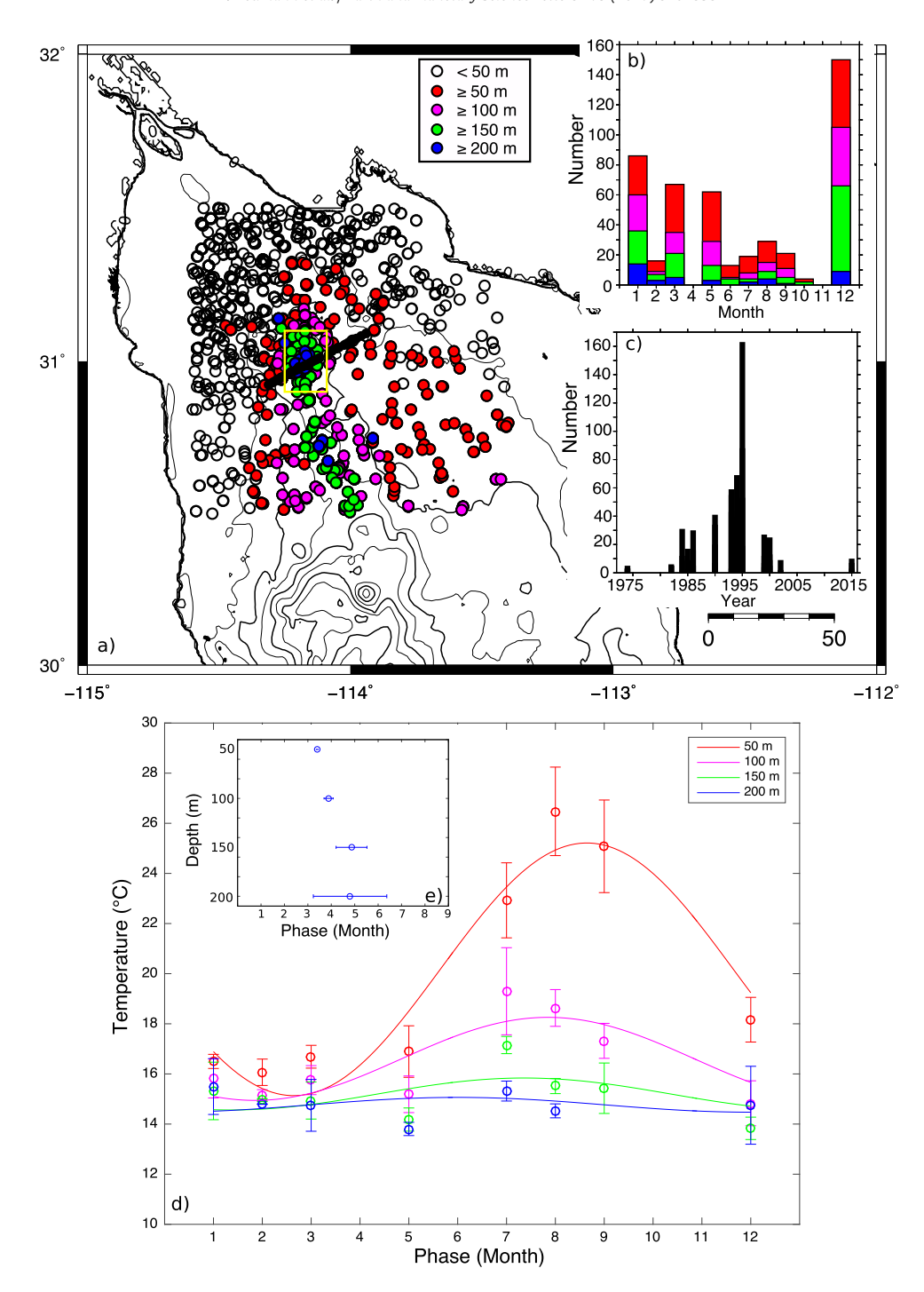


Fig. 4. a) CTD casts in the northern Gulf of California (Levitus et al., 2013; Godínez et al., 2013) and are color coded by their maximum depth. Open circles represent CTD cast with depth less than 50 m. Black filled circles show heat flow measurements. Circles are color coded according to the depth of deepest measurement. Yellow rectangle shows location of CTD casts shown in Fig. 5. b) Histogram showing monthly distribution of CTD casts, and colors show maximum depth of casts. c) Histogram showing number of CTD casts by year. d) Average temperature-month (circles) with standard deviation for CTD casts. Curves show best fitting sinusoid with a period of one year to the average temperature. e) Optimum phase for fitted sinusoid as a function of depth. (For interpretation of the references to color in this figure, the reader is referred to the web version of this article.)

From (4) we can obtain an analytical expression for heat flow by taking the derivative and multiplying through by k_e ,

$$k_e \frac{\partial T}{\partial z} = \frac{k_e \Gamma_l \exp(\frac{\beta}{L} z)}{\exp(\beta)}.$$
 (7)

We evaluate this expression for surface heat flow, q_0 , at z = 0, and set the product $k_e\Gamma$ equal to the basal heat flow, q_b , we obtain,

$$q_b = q_0 \exp(\beta). \tag{8}$$

In this way, q_0 , can be expressed as a multiple of q_b , and with this ratio known, V_z can be expressed as a function of L, as follows

$$V_z(L) = \frac{k_e}{\phi \rho_w c_w L} \ln \left(\frac{q_b}{q_0} \right). \tag{9}$$

Fig. 8 shows the relationship between V_z and L appropriate for the western and eastern flank of the Wagner Basin, with $q_0/q_b = 1.5$ and 6, respectively. Here, we have assumed that the sediment corrected heat flow (\sim 150 mW m⁻²) in the central graben of the

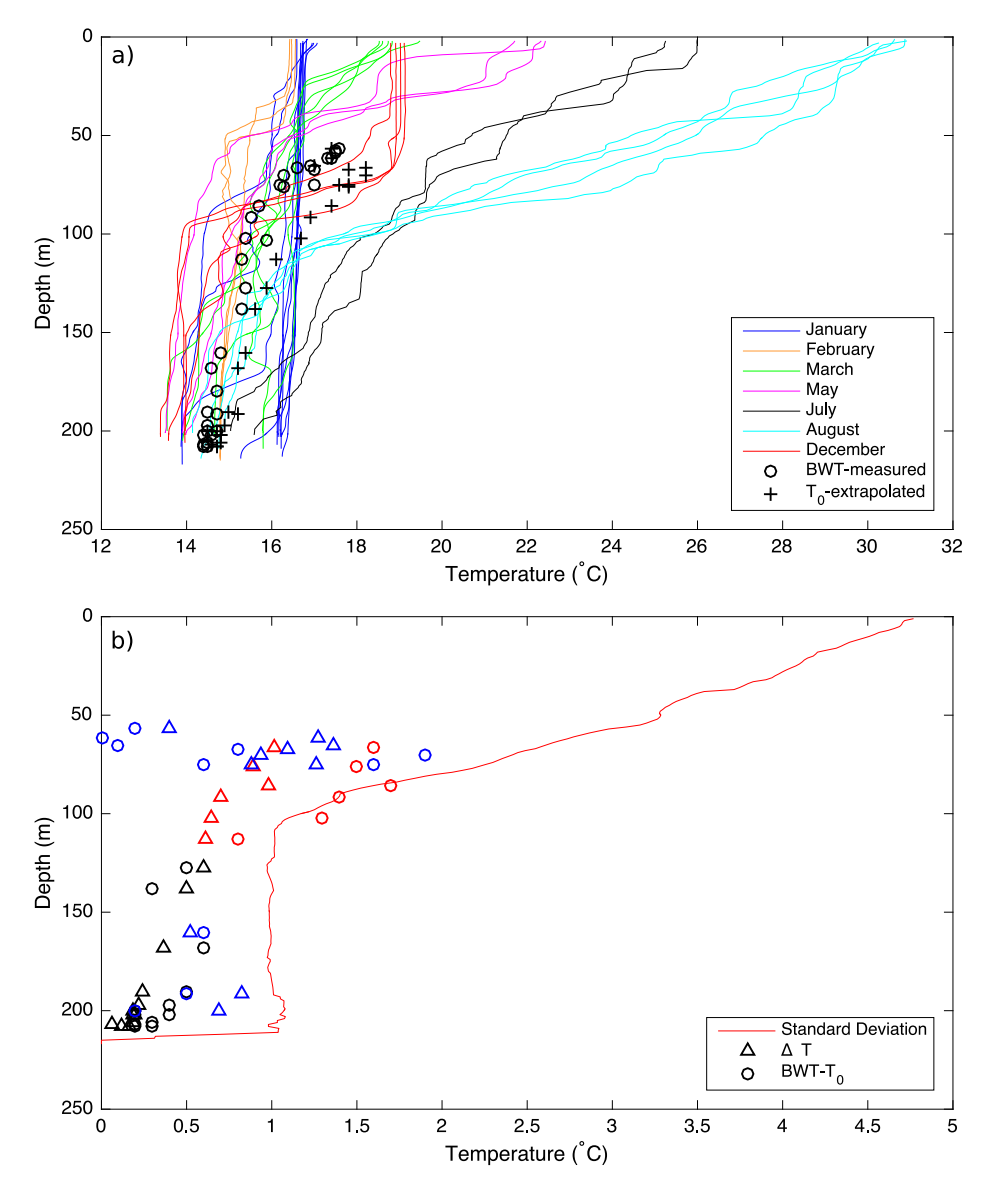


Fig. 5. a) Temperature profiles from CTD casts in the northern Gulf of California (yellow rectangle Fig. 4). Profiles are color coded by month of acquisition. Open circles show mean bottom water temperature (BWT) measured at top of the probe during each heat flow measurement (May, 2015). Crosses show seafloor temperature extrapolated from the data. b) Red line corresponds to one-standard deviation of the CTD measurements. Triangles show the best fitting amplitude of seasonal variation (ΔT) to the temperature-depth profiles. Circles show the difference between the BWT and extrapolated seafloor temperature (T_0). Circles and triangles are color coded by geographic position, red corresponds to the western margin, blue to the eastern margin, and black to the central basin. (For interpretation of the references to color in this figure, the reader is referred to the web version of this article.)

Table 2Parameter values for Porous Flow Calculation.

Parameter	Value		
Porosity, θ	0.2		
Fluid density, ρ_w	$1000 \mathrm{kg} \mathrm{m}^{-3}$		
Specific heat of fluid, c_w	4186 J kg ⁻¹ K ⁻¹		
Effective thermal conductivity, k_e	$2 \text{ W m}^{-1} \text{ K}^{-1}$		

Wagner basin corresponds with the background heat flow of the system q_b . Material parameters for this calculation are given in Table 2. Faults in the western and eastern flanks are observed to depths of \sim 1.75 km, which we take as estimate of L. Below this depth the Darcy velocity is relatively insensitive to L. This calculation leads to flow rate estimates of approximately 2 and 8 cm yr $^{-1}$ for the western and eastern flank, respectively. This model indicates that the larger heat flow observed along the eastern margin of the Wagner Basin could be attributed to greater flow rates, larger values of L, greater permeability along the fault conduits,

larger basal heat flux, or a combination of these factors. For example, if the flow velocity on the eastern flank is the same as that on the western flank, flow would need to originate at a depth of about 8.5 km. Because the horizontal variability (several km) is proportional to the source depth in steady state an L of 8.5 km may be too deep. The magnitude of flow also suggests that the heat source will be depleted over time. Both of these observations may be suggesting that this flow system is transient. Without independent evidence, such as geochemical indicators of fluid flow through the seafloor, our model is under constrained and necessarily non-unique.

4. Continental rupture?

A central question regarding the Wagner Basin is whether continental rupture is complete and seafloor spreading has started. In analogy with the Salton Trough and the Guaymas Basin (Fuis et al., 1984; Han et al., 2016; Kluesner and Lonsdale, 2008), we envision

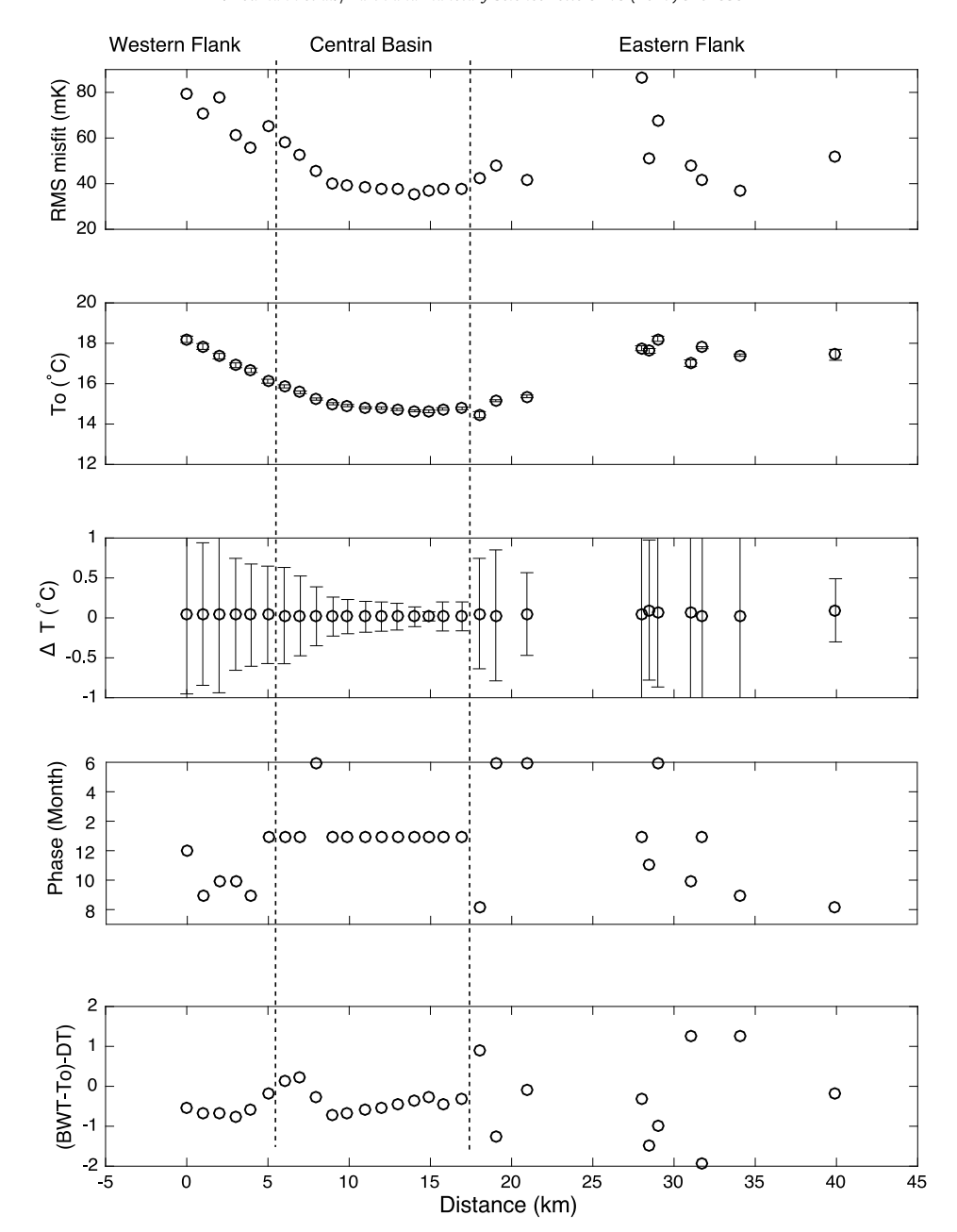


Fig. 6. Parameters resulting from inversion scheme as a function of distance. a) RMS misfit between the observed and predicted temperature. b) Long term seafloor temperature (T_0). Uncertainties show 95% confidence interval. c) Optimum amplitude of seasonal variation (ΔT) to the temperature-depth profiles with 95% confidence interval. d) Optimum phase. d) Circles show the difference between the BWT, extrapolated seafloor temperature (T_0) and amplitude of seasonal variation (T_0). Dashed lines show the limits of geographic position, corresponding to the western, eastern margin, and the central basin.

that the crust has a stratified structure consisting of sediments and metasediments overlying a layer of felsic and/or gabbroic material. The gabbroic material flows upwards and then, when the hydrostatic pressure equalizes with their surroundings, they flow out horizontally as sills. We consider the continental crust to be ruptured if gabbroic dikes reach the base of the metasediment layer and address this question using a two-pronged approach. First, we use isostatic considerations to make inferences about the crustal structure, and then use a thermal model to test if the heat flow data is consistent with diking to the base of the upper crust.

Because of the high heat flow and small free-air gravity anomalies associated with the Wagner Basin we assume it is in isostatic equilibrium. Our inferred crustal geometry is shown in Fig. 9a. For this situation seafloor depth can be expressed as (e.g., Lachenbruch and Morgan, 1990),

$$d = \frac{\rho_a - \rho_{uc}}{\rho_a - \rho_w} L_{uc} + \frac{\rho_a - \rho_{lc}}{\rho_a - \rho_w} L_{lc} - \frac{\rho_a}{\rho_a - \rho_w} H_0$$
 (10)

where ρ_a , ρ_{uc} , ρ_{lc} , and ρ_w are the densities of the asthenosphere, the upper crust, the lower crust, and water, respectively. L_{uc} and L_{lc} are the thicknesses of the upper and lower crust and H_0 is the buoyant height of sea level, taken to be 2.6 km based on the average depth of ridges and an asthenospheric density of 3200 kg m⁻³ (e.g., Lachenbruch and Morgan, 1990). We are interested in the thickness and density of the upper crust and lower crust. Sediment is seismically imaged to at least 7 km (González-Escobar et al., 2010) and receiver functions indicate that the total crustal thickness is 15 km (Lewis et al., 2001). A gravity model across the northern GC in the region of the Wagner Basin shows an upper crust of \sim 8 km with an average density of 2550 kg m⁻³ (Couch et al., 1991). This density is consistent with density logs

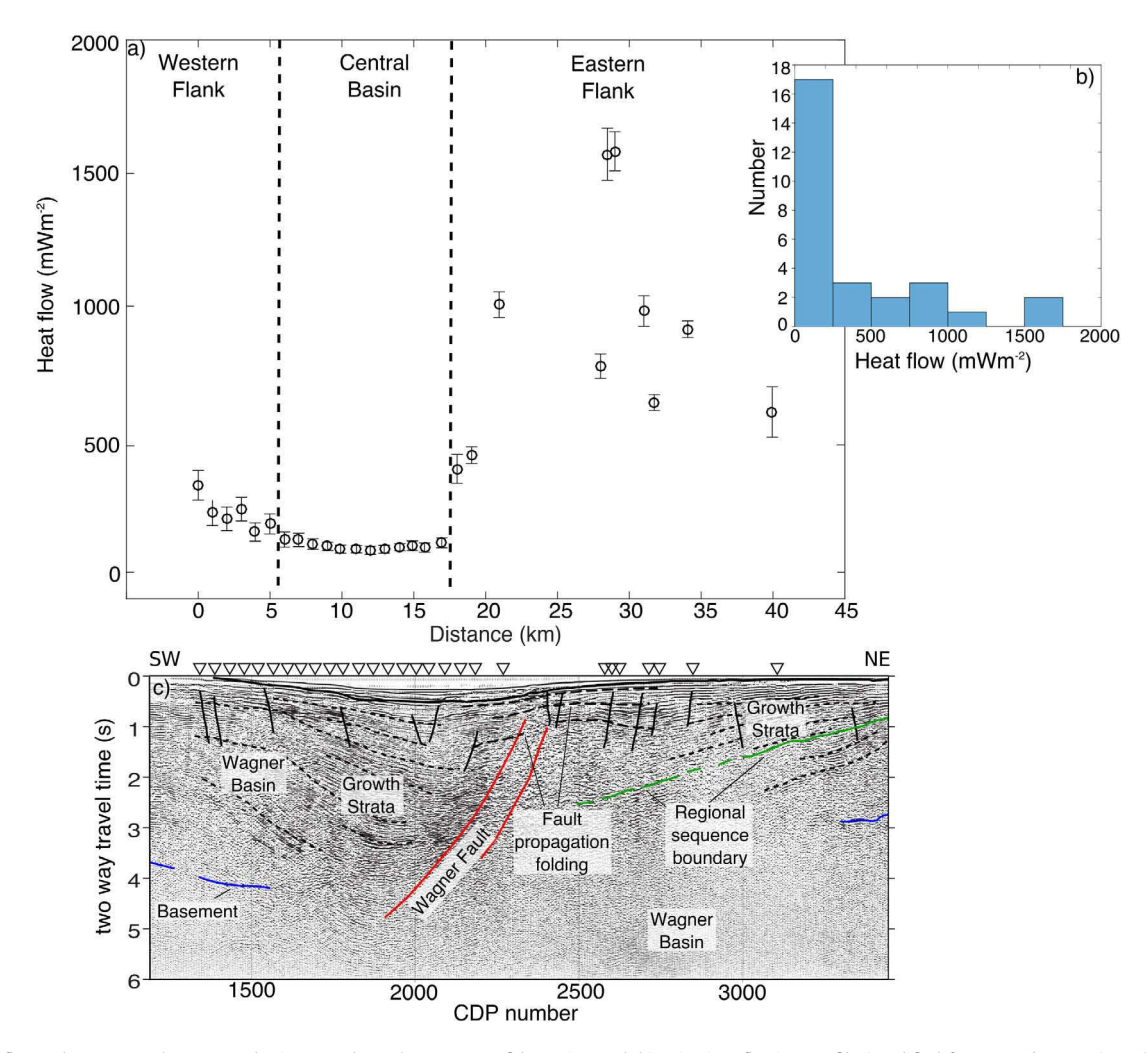


Fig. 7. a) Heat flow values across the Wagner basin. Error bars show 95% confidence interval. b) Seismic reflection profile (modified from Aragón-Arreola and Martín-Barajas, 2007). Red lines show Wagner fault. Black lines show faults across the basin, blue the acoustic basement, green the regional sequence boundary and triangles show heat flow measurements. (For interpretation of the references to color in this figure, the reader is referred to the web version of this article.)

from nearby boreholes that extend to depths of 4 km or more, and which show a compaction trend suggesting that the maximum sediment density is no more than approximately 2500 kg m $^{-3}$ (Pacheco et al., 2006). The gravity model suggests a metasedimentary lower crust with a density of 2630 kg m⁻³ and is consistent with a similar gravity model over the Salton Trough (Fuis et al., 1984). Fig. 9b shows the isostatic seafloor depth as a function of upper crustal thickness and lower crustal density for a sediment density of 2550 kg m⁻³. If continental rupture has occurred then the lower crust would have a density between 2900 and 3000 kg m⁻³, consistent with a mafic lower crust, and require a sediment thickness between \sim 8 and 8.5 km as indicated by point A (Fig. 9b). This thickness is consistent with gravity models and indicates that the observed bathymetry is consistent with a gabbroic lower crust, and that a felsic layer in the lower crust is not required. However, a gabbroic lower crust could also be due to underplating.

We now investigate whether the heat flow data is consistent with gabbroic dikes through the lower crust or underplating at the base of the crust using the approach of Lachenbruch et al. (1985). They developed one-dimensional steady-state thermal models of extension to test if continental rupturing had completed in the Salton Trough. In these models, extension is accompanied by sedimentation at rate s, and either diking or underplating at rate b. The crustal thickness, a, satisfies the following differential equation in which the first term on the right represents the rate of crustal

thinning caused by extension and the second and third terms are the rates of thickening by sedimentation and under plating, respectively (Lachenbruch et al., 1985),

$$\frac{da}{dt} = -\dot{\varepsilon}a + s + b,\tag{11}$$

where ε is the strain rate. Assuming steady state, equation (11) reduces to,

$$a = S + B, (12)$$

where S is the portion of the crust whose thinning is compensated by sedimentation and B is the portion compensated by underplating. Even if extensional strain rate $\dot{\varepsilon}$ varies with time and horizontal position, S and B will remain constant as long as the accumulation rates remain proportional to strain rate (Lachenbruch et al., 1985).

Lachenbruch et al. (1985) parameterized their model in terms of the strain rate and normalized sedimentation rate, S', defined as the ratio of sedimentation rate to combined rate of sedimentation and under plating,

$$S' = \frac{S}{S+B}. (14)$$

Based on the isostatic result above S' is approximately 0.5. Assuming rifting has occurred over the past 6 Myr with a total orthogonal offset of \sim 255 km (Oskin et al., 2001), we estimate a strain rate

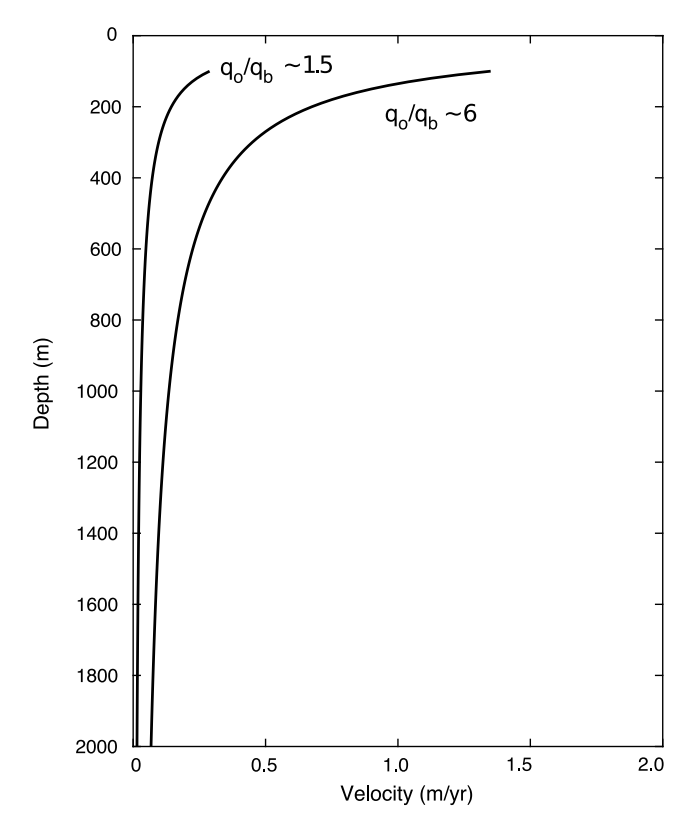


Fig. 8. Darcy velocity as a function of flow length, L for different ratios of the basal heat flow, q_h , and the observed heat flow q_0 .

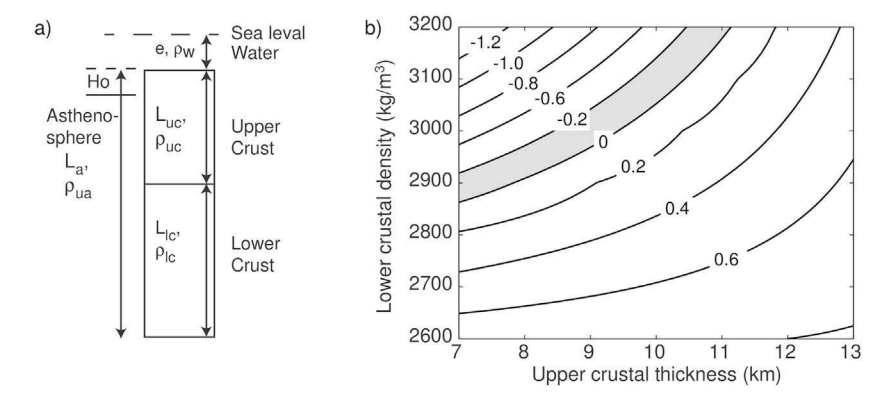


Fig. 9. Isostatic model for the Wagner Basin. a) Schematic representation of the crustal comprising the Wagner Basin. b) Predicted bathymetry/elevation in km for the Wagner Basin as a function of lower crustal density and upper crustal thickness. In the diagram the upper crustal density is taken as 2550 kg m⁻³ and the total crustal thickness is 15 km (Lewis et al., 2001). Shaded are shows permissible combinations of lower crustal density and upper crustal thickness.

of about $1\times10^{-15}~{\rm s}^{-1}$ for the underplating model. With these parameters we compute the geotherm due to underplating (Fig. 10a) using Equation B11 in Lachenbruch et al. (1985). In this equation the heat released by the underplated magma is modeled as a plane source with a discontinuity in conductive heat flow. We assume the base of the crust is kept isothermal at the gabbro solidus temperature of $1010\,^{\circ}$ C. Note that this condition is not contingent on the heat flow entering from the mantle.

In the alternative scenario, complete rupturing of the continental lithosphere implies that the dikes cut through the lower crust reaching the bottom of the sediments (Fig. 10b). In this case the geotherm is calculated using Equation B19 in Lachenbruch et al. (1985) that accounts for heat lost by the dike as it cools in place and heat lost by its magma during its rise. In this scenario we assume extension takes place over a width of 5 km, similar to oceanic spreading systems. This smaller region of extension leads

to a higher strain rate of $5\times 10^{-14}~\text{s}^{-1}$, more consistent with typical plate boundary strain rates.

The geotherms for distributed and focused extension are shown in Fig. 10c. The increase in temperature with depth for the focused extension model is more rapid than the distributed extension model because the depth to melt is much shallower; 8.5 km as opposed to 15 km. If there is diking and it has not yet reached the base of the metasediments the geotherm would fall between these two end member models.

We estimate the heat flow by computing the thermal gradient and multiplying by the thermal conductivity. In the northern Salton Sea, Sass and Elders (1986) report thermal conductivities of 1.8 W m $^{-1}$ K $^{-1}$ for siliclastics with a mean porosity of 26%. These siliclastics are similar to those found in the Wagner Basin. The corresponding grain thermal conductivity is 2.8 W m $^{-1}$ K $^{-1}$. A compaction curve based on Athy's law with a surface porosity of 70% and a compaction factor of 0.46 km $^{-1}$, appropriate

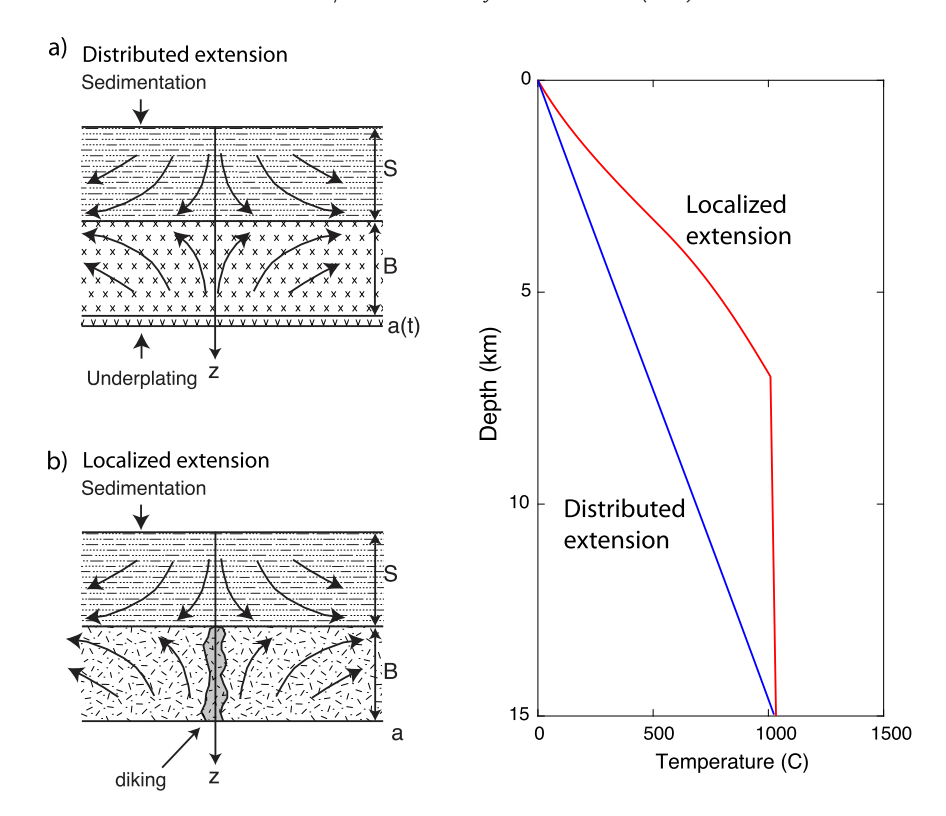


Fig. 10. a) Pure shear and b) diking model of crustal extension (modified from Lachenbruch et al., 1985). In the diagram *S* refers to sediment and *B* is the thickness of underplated material. c) Geotherms corresponding to pure shear (blue) and diking (red) that includes the effects of sedimentation and cooling and crystallization of gabbro. (For interpretation of the references to color in this figure, the reader is referred to the web version of this article.)

for this mixture, yields sediment thermal conductivities that increase from about 0.9 W m $^{-1}$ K $^{-1}$ at the surface to a maximum of 2.7 W m $^{-1}$ K $^{-1}$ at 8.5 km.

At the surface the geotherms corresponding to distributed and localized extension lead to heat flow values of approximately 105 and 165 mW m $^{-2}$, respectively. Sass and Elders (1986) report an average radioactive heat production of 1 μ W m $^{-3}$ for the Salton Trough and we think this value is appropriate for Wagner Basin sediments. This value of heat production contributes 8 mW m $^{-2}$ to the surface heat flow and brings our predicted heat flow values to 113 and 173 mW m $^{-2}$, respectively, a 35% difference in heat flow. Because sedimentation is included in this model we compare these values against our heat flow values uncorrected for sedimentation. The heat flow value for distributed extension compares very well with our observed heat flow of 99 mW m $^{-2}$ and is well within our 95% uncertainty of 14 mW m $^{-2}$.

5. Discussion

We suggest that an observed heat flow of approximately 99 \pm 14 mW m⁻² and a sedimentation corrected value of \sim 150 \pm 21 mW m⁻² is appropriate for the central Wagner Basin. The largest uncertainties of our heat flow analysis over the central Wagner Basin stems from our BWT variation correction and the sediment correction. Our sensitivity analysis in supplemental information 1 suggests we can recover heat flow estimates to a few percent in the presence of realistic BWT variations. Comparisons of our values against bottom hole temperatures from nearby boreholes and at depths well below the influence of BWT variations are within the 95% uncertainty of our observed heat flow. Bottom hole temperatures from PEMEX (Fig. 1) are 273 °C at 5591 m, 238 °C at 4930 m, and 159 °C at 3302 m, respectively (Espinoza-Ojeda et al., 2017). These values yield an average thermal gradient of 49.5 °C km⁻¹ and a heat flow value of 89 mW m⁻² uncorrected for sedimentation. However, comparisons between our estimated basal heat flow of 150 \pm 21 mW m⁻² and a Curie isotherm analysis suggests we may be overestimating the sediment correction. The Curie isotherm analysis suggests a basal heat flow of 126 mW m⁻² (Sanchez-Zamora et al., 1991). We note the consistency of our sediment corrected heat flow values, the bottom hole temperatures from depths of approximately 5 km and the Curie isotherm analysis based on a depth of approximately 11 km. The consistency of these results suggests that significant quantities of heat are not being advected from the central Basin to either the western or eastern flanks.

We hypothesize that the high and scattered heat flow values on the western and eastern margin of the Wagner Basin in terms of advective fluid flow. The Wagner basin is bounded on the east by the Cerro Prieto fault and on the west by the Percebo and Consag faults (González-Escobar et al., 2010). These basin bounding listric normal faults are active and transfer oblique extension between the Wagner and Consag basins. The footwalls of these faults are dissected by numerous faults. We hypothesize that these faults are permeable and focus fluid flow. The main evidence that these anomalies are not due to a conductive source is the large variation over spatial scales less than a few kilometers. If these anomalies were due to a conductive heat source, the source would need to be very close to the seafloor and there is no evidence for such a source. Testing this hypothesis required additional heat flow data in and out of the plane of our transect and geochemical data.

Moreover, we argue that the lower crust beneath the Wagner Basin has not yet fully ruptured and that underplating is occurring at $\sim\!15$ km, the base of the crust. We suggest that underplating may be an important process in weakening the lithosphere just prior to complete rupture and the onset of seafloor spreading. As the underplated material solidifies and cools it warms and weakens the overlying crust. For the Wagner basin, we envision underplating as a precursor to diking during continental rupture.

These models, of course, are clearly an approximation because in reality neither the steady state nor one-dimensional assumptions are completely valid. However, relaxing these assumptions requires data for the Wagner Basin that does not yet exist, such as basement structure, rifting and subsidence history. The thermal time constant associated with diking at 8.5 km is approximately 2 Myr; therefore the steady state equation may not be a bad representation. In contrast, the time constant associated with underplating at 15 km is approximately 7 Myr and given that strain localized approximately 6 Ma, the observed heat flow associated with underplating may be underestimated. The one-dimensional assumption also leads to uncertainties in our analysis. The central part of the Wagner Basin, which we interpret to have seafloor heat flow indicative of conductive conditions at depth, is about 15 km across giving a width/depth ratio of about one for underplating, and may also lead to an underestimate of the surface heat flow. However, given the relatively uniform values of heat flow across the central Wagner Basin, this assumption may be adequate.

Even though our simple pure shear model is in agreement with more sophisticated thermomechanical models, supporting the idea of distributed deformation (Persaud et al., 2016), there is evidence of new oceanic crust being produced under the depocenters of the Consag and Delfin Basins farther south (Martin-Barajas et al., 2013; González-Escobar et al., 2014). These authors note the presence of a large amplitude reflector at the base of the sediments at a depth of \sim 4 km, which they interpret as an igneous intrusion. Moreover, south of the Wagner Basin, the San Pedro Mártir fault has been interpreted as a large detachment suggesting simple shearing by low angle detachments. These finding suggests that basins in the northern GC are experiencing contrasting modes of extension and thermal regimes. Understanding the contrasting modes of extension in the northern GC is important to understanding its tectonics, rifting processes and is of economic relevance to the geothermal industry.

In this last regard, our regional value of 150 \pm 21 mW m⁻² across the central Basin with an area of approximately 1330 km² yields a heat output of approximately 200 MW. The throughput of the eastern bounding fault and uplifted block, by comparison, is tenfold that of the axial depression.

6. Conclusions

On the basis of our analysis we conclude the following:

- 1. Conductive heat flow, corrected for sedimentation over the Wagner Basin is about 150 \pm 21 mW m $^{-2}$. This value is consistent with 126 mW m $^{-2}$ based on a Curie isotherm analysis (Sanchez-Zamora et al., 1991) but over an order of magnitude less than suggested by Prol-Ledesma et al. (2013).
- 2. The conductive heat loss along the profile varies dramatically. On the western flank, it has a median of \sim 220 mW/m², in the central basin \sim 99 mW/m² and on the eastern flank, where we observe abundant shallow faulting and it crosses the extension of the major Wagner Fault, a median value, for the ten 10 complete penetrations, has a value of \sim 889 mW/m².
- 3. Distributed and localized extension lead to different predictions of heat flow. Our heat flow results are consistent with underplating at a depth of 15 km.

Acknowledgements

Funding was provided by the following projects: CATEDRAS CONACYT project 2074 (RN-A), CONACYT CEMIE-Geo strategic project P-03 (RN-A), NSF OCE-1634536 (RH), and CONACYT CEMIE-Geo doctoral scholarship 290747 (FN). We thank the officers and crew of the R/V Alpha Helix. The authors are especially grateful

to Christian Mueller from FIELAX and Michael Hutnak from Right on Q for their invaluable help during data collection. Efrain Gomez and Guillermo Mendez are thanked for their assistance during the campaign as well as Sergio Arregui and Jose Mojarro for their technical support. We appreciate comments from Alejandra Sanchez for discussions about tidal mixing in the Gulf of California, and Demian Saffer and Liz Screation for discussions about compaction driven seepage. Finally we would like to thank Andy Fisher and an anonymous reviewer for their constructive comments.

Appendix A. Supplementary material

Supplementary material related to this article can be found online at https://doi.org/10.1016/j.epsl.2017.09.037.

References

- Alvarez-Borrego, S., Lara-Lara, J.R., 1991. The Physical Environment and Primary Productivity of the Gulf of California. Chapter 26: Part V. Physical Oceanography, Primary Productivity, Sedimentology.
- Aragón-Arreola, M., Martín-Barajas, A., 2007. Westward migration of extension in the northern Gulf of California. Mexico. Geology 35 (6), 571–574.
- Argote, M.L., Amador, A., Lavín, M.F., Hunter, J.R., 1995. Tidal dissipation and stratification in the Gulf of California. J. Geophys. Res., Oceans 100 (C8), 16103–16118.
- Contreras, J., Martín-Barajas, A., Herguera, J.C., 2005. Subsidence of the Laguna Salada Basin, northeastern Baja California, Mexico, inferred from Milankovitch climatic changes. Geoffs. Int. 44 (1), 103.
- Couch, R.W., Ness, G.E., Sanchez-Zamora, O., Calderón-Riveroll, G., Doguin, P., Plawman, T., Coperude, S., Huehn, B., Gumma, W., 1991. Gravity anomalies and crustal structure of the Gulf and Peninsular Province of the Californias. The Gulf and the Peninsular Province of the Californias. AAPG Mem. 47, 47–70.
- DeMets, C., 1995. A reappraisal of seafloor spreading lineations in the Gulf of California: implications for the transfer of Baja California to the Pacific Plate and estimates of Pacific-North America motion. Geophys. Res. Lett. 22 (24), 3545–3548.
- Di Luccio, F., Persaud, P., Clayton, R.W., 2014. Seismic structure beneath the Gulf of California: a contribution from group velocity measurements. Geophys. J. Int. 199 (3), 1861–1877.
- Dorsey, R.J., 2010. Sedimentation and crustal recycling along an active oblique-rift margin: Salton Trough and northern Gulf of California. Geology 38 (5), 443–446.
- Dorsey, R.J., Fluette, A., McDougall, K., Housen, B.A., Janecke, S.U., Axen, G.J., Shirvell, C.R., 2007. Chronology of Miocene–Pliocene deposits at Split Mountain Gorge, southern California: a record of regional tectonics and Colorado River evolution. Geology 35 (1), 57–60.
- Espinoza-Ojeda, O.M., Prol-Ledesma, R.M., Iglesias, E.R., Figueroa-Soto, A., 2017. Update and review of heat flow measurements in México. Energy 121, 466–479.
- Fuis, G.S., Kohler, W.M., 1984. Crustal structure and tectonics of the Imperial Valley region, California. In: Rigsby, C.A. (Ed.), The Imperial Basin—Tectonics, Sedimentation and Thermal Aspects: Society of Economic Paleontologists and Mineralogists, Pacific Section, Annual Meeting, Field Trip Guidebook, vol. 40, pp. 1–13.
- Fuis, G.S., Mooney, W.D., Healy, J.H., McMechan, G.A., Lutter, W.J., 1984. A seismic refraction survey of the Imperial Valley region, California. J. Geophys. Res., Solid Earth 89 (B2), 1165–1189.
- Godínez, V., Lavín, M., Galindo-Bect, M., Sánchez-Velasco, L., 2013. Datos Hidrográficos en el Alto Golfo de California: Campaña PANGAS-1306 (11 al 21 de junio del 2013). Informe ténico 106556. Departamento de Oceanografía Física, CICESE. 136 pp.
- González-Escobar, M., Aguilar-Campos, C., Suárez-Vidal, F., Martín-Barajas, A., 2009. Geometry of the Wagner basin, upper Gulf of California based on seismic reflections. Int. Geol. Rev. 51 (2), 133–144.
- González-Escobar, M., Suárez-Vidal, F., Hernández-Pérez, J.A., Martín-Barajas, A., 2010. Seismic reflection-based evidence of a transfer zone between the Wagner and Consag basins: implications for defining the structural geometry of the northern Gulf of California. Geo Mar. Lett. 30 (6), 575–584.
- González-Escobar, M., Suárez-Vidal, F., Sojo-Amezquita, A., Gallardo-Mata, C.G., Martin-Barajas, A., 2014. Consag basin: northern Gulf of California, evidence of generation of new crust, based on seismic reflection data. Int. Geol. Rev. 56 (11), 1315–1331.
- González-Fernández, A., Dañobeitia, J.J., Delgado-Argote, L.A., Michaud, F., Córdoba, D., Bartolomé, R., 2005. Mode of extension and rifting history of upper Tiburón and upper Delfín basins, northern Gulf of California. J. Geophys. Res., Solid Earth 110 (B1).
- Han, L., Hole, J.A., Stock, J.M., Fuis, G.S., Kell, A., Driscoll, N.W., Kent, G.M., Harding, A.J., Rymer, M.J., González-Fernández, A., Lázaro-Mancilla, O., 2016. Continental rupture and the creation of new crust in the Salton Trough rift, Southern California and northern Mexico: results from the Salton Seismic Imaging Project. J. Geophys. Res., Solid Earth 121 (10), 7469–7489.

- Hartmann, A., Villinger, H., 2002. Inversion of marine heat flow measurements by expansion of the temperature decay function. Geophys. J. Int. 148 (3), 628–636.
- Helenes, J., Carreño, A.L., Carrillo, R.M., 2009. Middle to late Miocene chronostratigraphy and development of the northern Gulf of California. Mar. Micropaleontol. 72 (1), 10–25.
- Henyey, T.L., Bischoff, J.L., 1973. Tectonic elements of the northern part of the Gulf of California. Geol. Soc. Am. Bull. 84 (1), 315–330.
- Klitgord, K.D., Mudie, J.D., Bischoff, J.L., Henyey, T.L., 1974. Magnetic anomalies in the northern and central Gulf of California. Geol. Soc. Am. Bull. 85 (5), 815–820.
- Kluesner, J., Lonsdale, P., 2008. Young Saucer-Shaped Sills Within Rapidly Accumulated Sediments of the Central Gulf of California. In: AGU Fall Meeting Abstracts.
- Lachenbruch, A.H., Morgan, P., 1990. Continental extension, magmatism and elevation; formal relations and rules of thumb. Tectonophysics 174 (1–2), 39–62.
- Lachenbruch, A.H., Sass, J.H., Galanis, S.P., 1985. Heat flow in southernmost California and the origin of the Salton Trough. J. Geophys. Res., Solid Earth 90 (B8), 6709–6736.
- Larson, P.A., Mudie, J.D., Larson, R.L., 1972. Magnetic anomalies and fracture-zone trends in the Gulf of California. Geol. Soc. Am. Bull. 83 (11), 3361–3368.
- Lavín, M.F., Marinone, S.G., 2003. An overview of the physical oceanography of the Gulf of California. In: Nonlinear Processes in Geophysical Fluid Dynamics. Springer, Netherlands, pp. 173–204.
- Levitus, S., Antonov, J.I., Baranova, O.K., Boyer, T.P., Coleman, C.L., Garcia, H.E., Grodsky, A.I., Johnson, D.R., Locarnini, R.A., Mishonov, A.V., Reagan, J.R., 2013. The world ocean database. J. Data Sci. 12 (0), WDS229–WDS234.
- Lewis, J.L., Day, S.M., Magistrale, H., Castro, R.R., Rebollar, C., Astiz, L., Eakins, J., Vernon, F.L., Brune, J.N., 2001. Crustal thickness of the peninsular ranges and gulf extensional province in the Californias. J. Geophys. Res. 106 (B7), 13–599.
- Lister, C.R.B., 1979. The pulse-probe method of conductivity measurement. Geophys. I. Int. 57 (2), 451–461.
- Lizarralde, D., Axen, G.J., Brown, H.E., Fletcher, J.M., González-Fernández, A., Harding, A.J., Holbrook, W.S., Kent, G.M., Paramo, P., Sutherland, F., Umhoefer, P.J., 2007. Variation in styles of rifting in the Gulf of California. Nature 448 (7152), 466–469.
- Lonsdale, P., 1989. Geology and tectonic history of the Gulf of California. The eastern Pacific Ocean and Hawaii. Boulder, Colorado. Geological Society of America, Geology of North America, v. N, pp. 499–521.
- Lonsdale, P., 1991. Structural patterns of the Pacific floor offshore of peninsular California. In: The Gulf and Peninsular Province of the Californias, vol. 47, pp. 87–125.
- Martín-Barajas, A., González-Escobar, M., Fletcher, J.M., Pacheco, M., Oskin, M., Dorsey, R., 2013. Thick deltaic sedimentation and detachment faulting delay the onset of continental rupture in the Northern Gulf of California: analysis of seismic reflection profiles. Tectonics 32 (5), 1294–1311.
- Montes, J.M., Lavín, M.F., Parés-Sierra, A.F., 2015. Seasonal heat and salt balance in the upper Gulf of California. J. Coast. Res. 32 (4), 853–862.
- Oskin, M., Stock, J., 2003. Marine incursion synchronous with plate-boundary localization in the Gulf of California. Geology 31 (1), 23–26.

- Oskin, M., Stock, J., Martín-Barajas, A., 2001. Rapid localization of Pacific-North America plate motion in the Gulf of California. Geology 29 (5), 459–462.
- Pacheco, M., Martín-Barajas, A., Elders, W., Espinosa-Cardeña, J.M., Helenes, J., Segura, A., 2006. Stratigraphy and structure of the Altar basin of NW Sonora: implications for the history of the Colorado River delta and the Salton trough. Rev. Mex. Cienc. Geol. 23 (1), 1–22.
- Pérez, G.A., 1980. Exploración petrolera de la porción noroccidental del Golfo de California. Boletin de la Asociación Mexicana de Geofísicos de Exploración, vol. 21, pp. 81–128.
- Persaud, P., Stock, J.M., Steckler, M.S., Martín-Barajas, A., Diebold, J.B., González-Fernández, A., Mountain, G.S., 2003. Active deformation and shallow structure of the Wagner, Consag, and Delfín Basins, northern Gulf of California, Mexico. J. Geophys. Res., Solid Earth 108 (B7).
- Persaud, P., Di Luccio, F., Clayton, R.W., 2015. Rayleigh wave dispersion measurements reveal low-velocity zones beneath the new crust in the Gulf of California. Geophys. Res. Lett. 42 (6), 1766–1774.
- Persaud, P., Tan, E., Contreras, J., Lavier, L., 2016. A bottom-driven mechanism for distributed faulting in the Gulf of California rift. Tectonophysics.
- Plattner, C., Malservisi, R., Dixon, T.H., LaFemina, P., Sella, G.F., Fletcher, J., Suarez-Vidal, F., 2007. New constraints on relative motion between the Pacific plate and Baja California microplate (Mexico) from GPS measurements. Geophys. J. Int. 170 (3), 1373–1380.
- Prol-Ledesma, R.M., Torres-Vera, M.A., Rodolfo-Metalpa, R., Ángeles, C., Deveze, C.H.L., Villanueva-Estrada, R.E., Shumilin, E., Robinson, C., 2013. High heat flow and ocean acidification at a nascent rift in the northern Gulf of California. Nat. Commun. 4, 1388.
- Sanchez-Zamora, O., Doguin, P., Couch, R.W., Ness, G.E., 1991. Magnetic anomalies of the Northern Gulf of California: structural and thermal interpretations. In: The Gulf and Peninsular Provinces of the Californias, vol. 47, pp. 377–401.
- Sass, J.H., Elders, W.A., 1986. Salton Sea scientific drilling project: scientific program. Trans., Geotherm. Resour. Counc. 10, 473–478.
- Stock, J.M., Lee, J., 1994a. Do microplates in subduction zones leave a geological record? Tectonics 13 (6), 1472–1487.
- Stock, J.M., Lee, J., 1994b. Do microplates in subduction zones leave a geological record? Tectonics 13 (6), 1472–1487.
- Umhoefer, P.J., 2011. Why did the Southern Gulf of California rupture so rapidly?— Oblique divergence across hot, weak lithosphere along a tectonically active margin. GSA Today 21 (11), 4–10.

Further Reading

Athy, L.F., 1930. Density, porosity, and compaction of sedimentary rocks. Am. Assoc. Pet. Geol. Bull. 14 (1), 1–24.